Large-eddy simulation and Reynolds-averaged Navier-Stokes modeling of three Rayleigh-Taylor mixing configurations with gravity reversal

Brandon E. Morgan
Lawrence Livermore National Laboratory, Livermore, California 94550, USA

(Received 12 May 2022; accepted 18 July 2022; published 1 August 2022)

High-fidelity large-eddy simulation (LES) is performed of Rayleigh-Taylor (RT) mixing in three different configurations involving gravity reversal. In each configuration, LES results are compared with one-dimensional Reynolds-averaged Navier-Stokes (RANS) results, and a deficiency in a commonly used transport equation for the mass-flux velocity, a_j, is identified. In the first configuration, a classical two-component RT mixing layer is allowed to develop before it is subjected to rapid acceleration reversal. In the second configuration, a three-component RT mixing layer with an intermediate density layer is allowed to develop before being subjected to rapid acceleration reversal. Finally, in the third configuration, a light layer is interposed between two heavy layers; in this configuration, only one interface is RT-unstable at a time as it undergoes rapid acceleration reversal. In all cases, a commonly used buoyancy production closure in the a_j transport equation is shown to lead to significant over-prediction of mixing layer growth after gravity reversal. An alternative formulation for this closure is then presented which is shown to more accurately capture the stabilization effect of gravity reversal.

DOI: 10.1103/PhysRevE.106.025101

I. INTRODUCTION

Classical Rayleigh-Taylor (RT) instability occurs when two fluids of differing densities are subjected to an acceleration directed from the heavy fluid toward the light fluid. In such a configuration, perturbations at the interface between the two fluids grow, interact, and eventually transition to turbulence. RT-driven mixing occurs in a number of applications from astrophysical phenomenon to inertial confinement fusion (ICF) [1,2].

In ICF, RT instability often occurs at the gas-ablator interface, and turbulent mixing of these materials can contribute to degradation of target performance [3,4]. However in ICF applications, capsules are frequently subjected to complex acceleration histories, often leading to time periods with acceleration favorable to RT growth alternating with time periods of deceleration and partial interfacial stabilization [5]. For this reason, two-fluid RT instability with time-varying acceleration has been studied both experimentally and computationally by a number of previous researchers [6–12].

Since Reynolds-averaged Navier-Stokes (RANS) modeling approaches remain common within the ICF community, it is important that RANS models are capable of providing accurate prediction of RT mixing for complex accelerations. Recently, Braun and Gore [13] have presented a new approach for the Besnard-Harlow-Rauenzahn (BHR) family of RANS models [14–16] with the intent to better capture the behavior of RT mixing following acceleration reversal. Under this new approach, which Braun and Gore call the BHR-4 model, a gradient diffusion approximation is not used to close the turbulent species mass flux; instead, additional model transport equations are solved for each species mass flux. While this approach is shown to provide better agreement for RT flow with gravity reversal, it also adds significant complexity to the model.

As the present work will show, the inability of many RANS models to correctly capture mixing layer stabilization after gravity reversal seems to derive from treatment of the buoyancy production term in the mass-flux velocity (a_j) equation. Indeed, the k-L model [17,18] is a simple two-equation model which uses an algebraic closure for a_j. Later in Sec. III, it will be shown that the k-L model does not suffer from the same deficiency as subsequent extensions [19–24] in predicting the mixing width stabilization of two-fluid RT following gravity reversal. Of course, in more complicated flows such as those involving shocks, the more advanced models are still preferred. Therefore, a need exists to correct the observed deficiency in models that utilize a transport equation for a_j. Table I provides a brief summary of RANS models considered in the present work.

It is therefore with a motivation towards RANS model assessment and improvement that the present work examines the problem of RT mixing under gravity reversal. In particular, large-eddy simulation (LES) using a tenth-order accurate compact difference scheme is utilized to simulate three different configurations. In each case, LES results are compared with RANS results in order to assess and improve the capacity of RANS models to capture the effect of gravity reversal. In the first configuration, a classical two-component RT mixing layer is allowed to develop to turbulence before it is subjected to a rapid acceleration reversal. In the second configuration, a three-component RT mixing layer with an intermediate density layer (similar to the three-component configuration studied in [24]) is considered, which allows two unstable interfaces to develop before being subject to rapid acceleration reversal. Finally, in the third configuration, a light fluid is interposed between two heavy layers, creating a

TABLE I. Summary of RANS models considered.

Model	Description	Capabilities	Limitations
k-L [17]	Two-equation Boussinesq model	Self-similar growth for RT mixing Captures RT mixing layer stabilization following gravity reversal	Typically requires shock detection for Richtmyer-Meshkov (RM) growth at RT-stable interfaces Low-order approximation of spatial profiles Does not capture Reynolds stress anisotropy
k-L-a [19]	Three-equation extension of the *k-L* model, includes transport of mass-flux velocity a_i	Self-similar growth for RT mixing Does not require shock detection for RM growth at RT-stable interfaces	Fails to capture RT mixing layer stabilization following gravity reversal Low-order approximation of spatial profiles Does not capture Reynolds stress anisotropy
k-L-a-$\mathcal{C}$ [21,24]	Four-equation extension of the *k-L-a* model, includes transport of mass fraction covariances for reacting flows	Self-similar growth for RT mixing Does not require shock detection for RM growth at RT-stable interfaces Used to model heterogeneity of mixing (i.e., "mixedness")	Fails to capture RT mixing layer stabilization following gravity reversal Low-order approximation of spatial profiles Does not capture Reynolds stress anisotropy
k-ϕ*-L-a-*$\mathcal{C}$ [23,24]	Five-equation extension of the *k-L-a-*$\mathcal{C}$ model, developed for prediction of high-order spatial profiles while maintaining self-similar model calibration	Self-similar growth for RT mixing Does not require shock detection for RM growth at RT-stable interfaces Used to model heterogeneity of mixing (i.e., "mixedness") High-order spatial profiles	Fails to capture RT mixing layer stabilization following gravity reversal Does not capture Reynolds stress anisotropy
BHR-3.1 [16]	Five-equation Reynolds-stress transport model, includes transport equations for mass-flux velocity, density-specific-volume covariance *b*, transport and dissipation length scales	Reproduces expected RT and RM growth rates Captures Reynolds stress anisotropy in RT mixing Does not require shock-detection for RM growth at RT-stable interfaces	Fails to capture RT mixing layer stabilization following gravity reversal Low-order approximation of spatial profiles
BHR-4 [13]	Multispecies extension of BHR-3.1, includes transport equations for turbulent mass flux and density-mass-fraction covariance for each species	Reproduces expected RT and RM growth rates Captures Reynolds stress anisotropy in RT mixing Does not require shock detection for RM growth at RT-stable interfaces Captures RT mixing layer stabilization following gravity reversal	Low-order approximation of spatial profiles Significant increase in model cost and complexity Nontrivial methods required to maintain mass fraction realizability

situation in which one interface is initially stable and the other interface is initially unstable, before the system is subjected to a rapid acceleration reversal. Figure 1 schematically depicts the three cases in terms of the heavy density ρ_H, the light density ρ_L, and the intermediate density ρ_I.

The remainder of this paper is laid out as follows. First, in Sec. II, descriptions are given of the numerical models utilized in the present work. Descriptions of the governing equations, computational codes utilized, and the RANS models considered are given in Secs. II A, II B, and II C. Problem setup and initial conditions are discussed in Secs. II D and II E. Then, in Sec. III, results of LES and RANS simulations of the three configurations under consideration are presented and discussed. Finally in Sec. IV conclusions are drawn, and recommendations are made concerning the direction of future research.

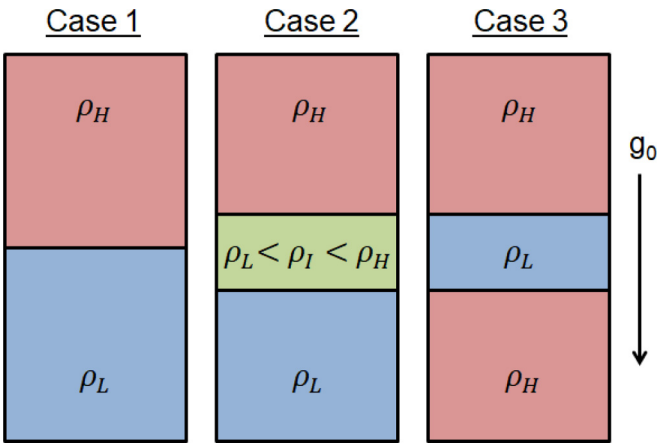

FIG. 1. Schematic representation of the three RT mixing configurations considered. The direction of the initial gravity vector is indicated as g_0.

II. NUMERICAL MODELS

A. The *Miranda* code

Three-dimensional LES calculations in the present work utilize the *Miranda* code to solve the compressible Navier-Stokes equations for a nonreacting, multicomponent mixture:

$$\frac{\partial \rho}{\partial t} + \frac{\partial(\rho u_i)}{\partial x_i} = 0, \tag{1}$$

$$\frac{\partial(\rho Y_\alpha)}{\partial t} + \frac{\partial(\rho Y_\alpha u_i)}{\partial x_i} = -\frac{\partial J_{\alpha,i}}{\partial x_i}, \tag{2}$$

$$\frac{\partial(\rho u_j)}{\partial t} + \frac{\partial(\rho u_i u_j)}{\partial x_i} = -\frac{\partial p}{\partial x_j} + \frac{\partial \sigma_{ij}}{\partial x_i} + \rho g_j, \tag{3}$$

$$\frac{\partial E}{\partial t} + \frac{\partial[(E+p)u_i]}{\partial x_i} = \frac{\partial(\sigma_{ij}u_i)}{\partial x_j} - \frac{\partial q_i}{\partial x_i} + \rho g_i u_i. \tag{4}$$

In Eqs. (1) through (4), ρ is density, t is time, u_i is the velocity vector, x_i is the spatial coordinate vector, Y_α is the mass fraction of species α, $J_{\alpha,i}$ is the diffusive mass flux of species α, p is pressure, σ_{ij} is the viscous stress tensor, g_j is a gravitational body force vector, E is the total energy, and q_i is the heat flux vector. The diffusive mass flux is given in terms of effective binary diffusion coefficients D_α as

$$J_{\alpha,i} = -\rho\left(D_\alpha \frac{\partial Y_\alpha}{\partial x_i} - Y_\alpha \sum_{\beta=1}^{N} D_\beta \frac{\partial Y_\beta}{\partial x_i}\right), \tag{5}$$

for k=1, 2, …, N total species. The viscous stress tensor is given by

$$\sigma_{ij} = 2\mu S_{ij} + \left(\beta - \frac{2}{3}\mu\right)\frac{\partial u_i}{\partial x_i}\delta_{ij}, \tag{6}$$

where μ is the shear viscosity, β is the bulk viscosity, δ_{ij} is the Kronecker delta, and S_{ij} is the strain rate tensor,

$$S_{ij} = \frac{1}{2}\left(\frac{\partial u_i}{\partial x_j} + \frac{\partial u_j}{\partial x_i}\right). \tag{7}$$

The heat flux vector is given in terms of the thermal conductivity κ, the temperature T, and species enthalpy h_α,

$$q_i = -\kappa\frac{\partial T}{\partial x_i} + \sum_{\alpha=1}^{N} h_\alpha J_{\alpha,i}. \tag{8}$$

Component temperature, enthalpy, and pressure are obtained through an ideal gas equation of state according to

$$p_\alpha = (\gamma_\alpha - 1)\rho_\alpha e_\alpha, \tag{9a}$$

$$T_\alpha = \frac{e_\alpha}{c_{v,\alpha}}, \tag{9b}$$

$$h_\alpha = \gamma_\alpha e_\alpha, \tag{9c}$$

where $c_{v,\alpha}$ is the specific-heat coefficient at constant volume for component α, and γ_α is the ratio of specific heats coefficients. Using an assumption of pressure and temperature equilibrium, an iterative process is used to solve for component volume fractions, v_α, which allows the determination of partial densities and energies according to

$$\rho_\alpha = \frac{Y_\alpha \rho}{v_\alpha} \tag{10}$$

and

$$e = \frac{E}{\rho} - \frac{1}{2}u_i u_i = \sum_{\alpha=1}^{N} Y_\alpha e_\alpha\ . \tag{11}$$

Total pressure is then determined according to the mixture relationship

$$p = \sum_{\alpha=1}^{N} v_\alpha p_\alpha. \tag{12}$$

The governing equations above are solved with a tenth-order compact differencing scheme for spatial discretization and a fourth-order explicit Runge-Kutta scheme for temporal integration. *Miranda* has been utilized extensively in previous studies of compressible turbulent mixing [21,24–32]. To model the subgrid-scale transfer of energy, *Miranda* utilizes an artificial fluid LES approach in which artificial transport terms are added to the fluid viscosity, bulk viscosity, thermal conductivity, and molecular diffusivity [33,34] according to

$$\mu = \mu_f + \mu^*, \tag{13a}$$

$$\beta = \beta_f + \beta^*, \tag{13b}$$

$$\kappa = \kappa_f + \kappa^*, \tag{13c}$$

$$D_\alpha = D_{f,\alpha} + D^*_\alpha, \tag{13d}$$

where the subscript f denotes the fluid, or physical, contribution to the molecular transport property, and an asterisk superscript denotes the artificial contribution. The form of the artificial contributions utilized in the present work is the same as that utilized in earlier work by Morgan *et al.* [21,35]. Since the present study is focused on the high-Reynolds-number regime in which viscous length scales are significantly smaller than energy-containing structures, the approach of Olson *et al.* [28] is adopted, and fluid contributions to dynamic viscosity, bulk viscosity, thermal conductivity, and molecular diffusivity are taken to be zero (i.e., $\mu_f = \beta_f = \kappa_f = D_{f,\alpha} = 0$).

B. The *Ares* code

One-dimensional (1D) RANS calculations in the present work utilize the *Ares* code to solve the compressible RANS equations for a nonreacting, multicomponent mixture. For the majority of RANS models considered in the present work, gradient diffusion closures are utilized to close turbulent transport terms in the transport equations for species mass and internal energy, which results in a set of governing equations of the following form:

$$\frac{D\overline{\rho}}{Dt} = -\overline{\rho}\frac{\partial \widetilde{u}_i}{\partial x_i}, \tag{14}$$

$$\overline{\rho}\frac{D\widetilde{Y}_\alpha}{Dt} = \frac{\partial}{\partial x_i}\left(\frac{\mu_t}{N_Y}\frac{\partial \widetilde{Y}_\alpha}{\partial x_i}\right), \tag{15}$$

$$\overline{\rho}\frac{D\widetilde{u}_j}{Dt} = \overline{\rho}g_j - \frac{\partial \overline{p}}{\partial x_j} + \frac{\partial}{\partial x_i}(\overline{\rho}\tau_{ij}), \tag{16}$$

$$\overline{\rho}\frac{D\widetilde{e}}{Dt} = -\overline{p}\frac{\partial \widetilde{u}_i}{\partial x_i} - E_{\rm src} + \frac{\partial}{\partial x_i}\left(\frac{\mu_t}{N_e}\frac{\partial \widetilde{e}}{\partial x_i}\right), \tag{17}$$

where

$$\frac{D}{Dt} \equiv \frac{\partial}{\partial t} + \widetilde{u}_i\frac{\partial}{\partial x_i}. \tag{18}$$

In Eqs. (14) through (17), μ_t is the eddy viscosity, N_Y and N_e are model-specific closure coefficients, $E_{\rm src}$ is a turbulent source that represents a transfer of energy between turbulence kinetic energy (TKE) and internal energy, and $\overline{\rho}\tau_{ij} \equiv -\overline{\rho u_i'' u_j''}$ is the Reynolds stress tensor. An overbar denotes Reynolds averaging, and a tilde denotes mass-weighted (Favre) averaging. An arbitrary scalar, f, is decomposed as

$$f = \overline{f} + f' = \widetilde{f} + f'', \tag{19}$$

where the Favre average is related to the Reynolds average according to

$$\widetilde{f} = \frac{\overline{\rho f}}{\overline{\rho}}. \tag{20}$$

For simulations in the present work, an ideal gas equation of state is used as described previously in Eqs. (9) through (12).

The *Ares* code solves the governing equations using an arbitrary Lagrangian-Eulerian (ALE) method with a second-order remap [36]. Explicit time integration is accomplished with a second-order predictor-corrector scheme [37], and spatial differences are computed with a nondissipative second-order finite element approach. A tensor artificial viscosity [38] is applied for the capturing of shocks and material discontinuities. Although *Ares* also boasts an adaptive mesh refinement (AMR) capability [39,40], it is not utilized in the present study. *Ares* has been applied previously in studies of canonical Richtmyer-Meshkov instability in both planar [30] and cylindrical [18] configurations. It has also been utilized extensively in multidimensional simulation of ICF targets and experiments [3,41–47] as well as in 1D simulations of turbulent mixing using RANS [19–24].

C. RANS models

Although the details may vary, a frequent approach to RANS modeling of turbulent mixing is to utilize transport equations for the TKE, k, and a turbulence length scale L [14,17,19–21,23,24,48–54]. The following equations represent a commonly encountered form of these transport equations:

$$\overline{\rho}\frac{Dk}{Dt} = \overline{\rho}\tau_{ij}\frac{\partial \widetilde{u}_i}{\partial x_j} + a_i\frac{\partial \overline{p}}{\partial x_i} - C_D\frac{\overline{\rho}(2k)^{3/2}}{L} + \frac{\partial}{\partial x_i}\left(\frac{\mu_t}{N_k}\frac{\partial k}{\partial x_i}\right), \tag{21}$$

$$\overline{\rho}\frac{DL}{Dt} = C_{L1}\overline{\rho}\sqrt{2k} + C_{L2}\overline{\rho}L\frac{\partial \widetilde{u}_i}{\partial x_i} + C_{L3}\overline{\rho}\tau_{ij}\frac{L}{k}\frac{\partial \widetilde{u}_i}{\partial x_j} + \frac{\partial}{\partial x_i}\left(\frac{\mu_t}{N_L}\frac{\partial L}{\partial x_i}\right), \tag{22}$$

where $a_i \equiv -\overline{u_i''}$ must be closed and is a model variable representing the mass-flux velocity, and C_D, C_{L1}, C_{L2}, C_{L3}, N_k, and N_L are model-specific coefficients.

1. Algebraic closure for mass-flux velocity

Models such as the k-L model of Dimonte and Tipton [17] utilize a gradient-diffusion approach to write the following algebraic closure for the mass-flux velocity:

$$a_i \approx -C_B\frac{\mu_t}{\overline{\rho}^2}\frac{\partial \overline{\rho}}{\partial x_i}, \tag{23}$$

where C_B is another model-specific coefficient. This form of closure can be well suited for capturing integral behavior of RT mixing such as the steady-state growth rate. However, it has been shown to have deficiencies in capturing countergradient mass flux in two-dimensional RT configurations such as the so-called "tilted-rocket rig" [49].

2. Transport equation for mass-flux velocity

An alternative approach for closing a_i is to solve a model transport equation such as the following:

$$\overline{\rho}\frac{Da_j}{Dt} = B_{a_j} - C_A\overline{\rho}a_j\frac{\sqrt{2k}}{L} - \tau_{ij}\frac{\partial \overline{\rho}}{\partial x_i} + \frac{\partial}{\partial x_i}\left(\frac{\mu_t}{N_a}\frac{\partial a_j}{\partial x_i}\right), \tag{24}$$

where B_{a_j} is a buoyancy production term typically written in the following way:

$$B_{a_j} \approx C_{B1}b\frac{\partial \overline{p}}{\partial x_j}. \tag{25}$$

In Eq. (25), $b \equiv -\overline{\rho'(\frac{1}{\rho})'}$ is the unitless density-specific-volume covariance requiring closure, and C_{B1} is a model coefficient. In three-equation models such as the k-L-a model [19] or the BHR-1 model [48], b is closed using an algebraic expression involving partial densities and volume fractions. In models such as the BHR-2 model [49] or the BHR-3 model [15,16], an additional transport equation is solved for b. Similarly, in models such as the k-L-a-V model [21] and the k-ϕ-L-a-V model [23], b is closed through relationship to the scalar variance, which is solved with a transport equation. Regardless of how b is closed, however, it is a strictly nonnegative quantity.

Now consider the case of a hydrostatic RT mixing layer in which $\nabla\overline{p} = -\overline{\rho}g_j$. Since b is nonnegative, when using Eq. (25), B_{a_j} will take the same sign as the pressure gradient, and as a result a_j will also take the same sign as the

pressure gradient, making the buoyancy production term in the k equation, $a_i \cdot \nabla \overline{p}$, positive as expected for unstable RT mixing. In the case of a rapid reversal of gravity, however, consider that the sign of Eq. (25) will also rapidly change. If this rapid change in the sign of B_{a_j} also results in a change in the sign of a_j, then $a_i \cdot \nabla \overline{p}$ will continue to be positive. In most cases, continued growth of k after gravity reversal would be nonphysical. Yet, it can be expected that models utilizing Eq. (25) will predict this behavior if they do not have a mechanism for rapidly dissipating b upon gravity reversal. For those three-equation models utilizing algebraic closures for b, it is clear that no such mechanism exists.

3. Alternative buoyancy production for a_j

Given the possibility of nonphysical behavior for models relying on Eq. (25), it is desirable to construct an alternative approach which would appropriately allow a_j to go to zero upon gravity reversal. With this property in mind, the following alternative approach is proposed, which follows a similar form to buoyancy production terms appearing in other model turbulence equations such as the ε equation for dissipation rate [55] or the scalar variance equation [24]:

$$B_{a_j} \approx C_{B2} a_j \frac{a_i}{2k} \frac{\partial \overline{p}}{\partial x_i}. \tag{26}$$

Notice that use of Eq. (26) effectively decouples b from the model. While this approach might seem counterintuitive, similarity analysis of the modified model can be used to illustrate how the effect of density variance is still captured in Eq. (26). As discussed by Morgan and Wickett for the k-L-a model [19], in the low-Atwood-number limit, the self-similar form of a_j for a 1D RT mixing layer is given by

$$a = -A\sqrt{2C_{B1}K_0} f, \tag{27}$$

where A is the conventional Atwood number, K_0 is the time-dependent self-similar TKE such that $k = K_0 f$, and $f(\chi) = 1 - \chi^2$ is the self-similar spatial function defined in terms of the self-similarity variable χ. The self-similar form of the algebraic b closure utilized by the k-L-a model is then given by

$$b = A^2 f. \tag{28}$$

Plugging back into Eqs. (25) and (26), it is straightforward to see that both will result in the same self-similar value

$$B_{a_j} = -C_{B1} A^2 \rho g f, \tag{29}$$

as long as $C_{B2} = 1$. Viewed through this lens, it is perhaps easier to see how in Eq. (26), $a_j a_i / 2k \sim b$. Indeed, the following realizability constraint [14] is expected and often explicitly enforced:

$$\frac{|a_i|^2}{2k} \leqslant b. \tag{30}$$

Thus, while the model variable b does not explicitly appear in Eq. (26), the scaling represented by b is still captured. Additional self-similarity analysis for the k-ϕ-L-a-$\mathcal{C}$ model [23,24] when using Eq. (26) is presented in Appendix A.

TABLE II. Summary of problem configurations. Densities in units of mg/cm^3.

Case	A_{32}	A_{21}	A_{31}	ρ_3	ρ_2	ρ_1
1	—	—	0.500	10.0	—	3.33
2	0.268	0.268	0.500	10.0	5.77	3.33
3	0.500	−0.500	0.000	10.0	3.33	10.0

D. LES problem setup and initial conditions

LES calculations are conducted on a computational mesh of dimension $2\pi \times 2\pi \times 4\pi$ cm^3 with the initial gravitational acceleration vector oriented in the negative z dimension. For configuration 1, the nominal fluid interface is located at $z = 0$ such that $\rho = \rho_L$ for $-2\pi \leqslant z < 0$, and $\rho = \rho_H$ for $0 \leqslant z \leqslant 2\pi$. Fluid densities are chosen such that $\rho_H = 0.01$ g/cm^3 and $A = 0.50$. For configuration 2, the initial thickness of the intermediate-density material is taken to be 1/8 of the domain size in z, such that the light material is initialized with ρ_L from $-2\pi \leqslant z < -\pi/4$, the intermediate-density material is initialized with ρ_I from $-\pi/4 \leqslant z < \pi/4$, and the heavy material is initialized with ρ_H from $\pi/4 \leqslant z \leqslant 2\pi$. Fluid densities in configuration 2 are chosen such that $\rho_H = 0.01$ g/cm^3, the Atwood number between heavy and light components is 0.50, and the Atwood number at the heavy-intermediate interface is equal to the Atwood number at the intermediate-light interface. For configuration 3, the initial thickness of the light material in between two layers of heavy material is also taken to be 1/8 of the domain size in z, such that heavy material is initialized with ρ_H from $-2\pi \leqslant z < -\pi/4$, the light material is initialized with ρ_L from $-\pi/4 \leqslant z < \pi/4$, and additional heavy material is initialized with ρ_H from $\pi/4 \leqslant z \leqslant 2\pi$. Densities in this configuration are taken such that $\rho_H = 0.01$ g/cm^3, and Atwood numbers at the unstable and stable interfaces are taken to be 0.50 and −0.50, respectively. Table II summarizes the three cases in terms of the generalized Atwood number A_{ij}, where an intermediate layer (if one exists) is assigned as component 2, and components 3 and 1 are those components surrounding the intermediate component to the top and bottom, respectively:

$$A_{ij} \equiv \frac{\rho_i - \rho_j}{\rho_i + \rho_j}. \tag{31}$$

Periodic boundary conditions are imposed in the x and y dimensions, and nonpenetrating wall boundaries are set at $z = -2\pi$ and $z = 2\pi$. A hydrostatic pressure field is specified such that the mixing layer remains nominally centered around $z = 0$. Constant mesh spacing is utilized in all dimensions, such that the number of grid points in the z dimension, N_z, is equal to twice the number of grid points in the x and y dimensions; in other words, $N_z = 2N_y = 2N_x$. For these simulations, $N_z = 1152$ for a total of about 382 million computational elements.

An initial perturbation is specified at each interface in Fourier space as a function of maximal and minimal wave

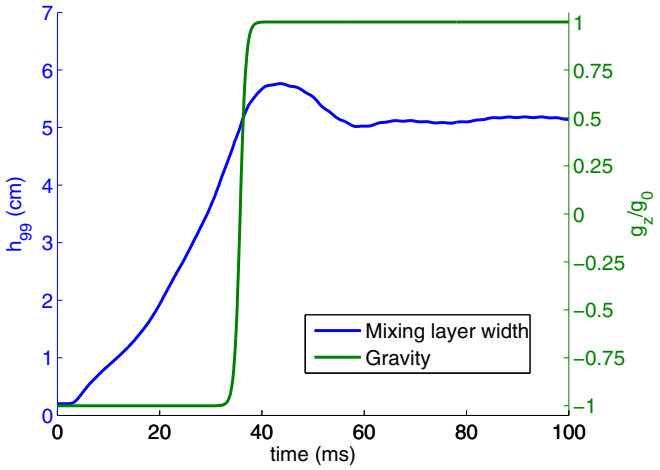

FIG. 2. Mixing layer width as a function of time (in blue) overplotted with gravity as a function of time (in green) for configuration 1.

numbers $\kappa_{\max}$ and $\kappa_{\min}$ according to

$$\xi(x,y) = \sum_{j=\kappa_{\min}}^{\kappa_{\max}} \sum_{k=\kappa_{\min}}^{\kappa_{\max}} \frac{\Delta}{\kappa_{\max} - \kappa_{\min} + 1} \cos(jx + \theta_{x,j}) \times \sin(ky + \theta_{y,k}), \tag{32}$$

where Δ indicates the mesh spacing and the phase shift vectors $\theta_{x,j}$ and $\theta_{y,k}$ are drawn from uniformly distributed random numbers between 0 and 2π. The mixture density at each interface at time $t = 0$ is then given by

$$\rho(x,y,z) = \rho_i + \frac{\rho_{i+1} - \rho_i}{2}\left[1 + \tanh\left(\frac{z - \xi(x,y)}{4\Delta}\right)\right]. \tag{33}$$

where the ρ_i indicates the density of the lower component at the interface, as summarized by Table II. A broadband initial perturbation spectrum is specified such that $\kappa_{\min} = 6$, and $\kappa_{\max} = 96$.

For each configuration, a rapid acceleration reversal is specified according to

$$g_z = g_0 \tanh\left(\frac{t - t_{\text{rev}}}{\Delta_{\text{rev}}}\right), \tag{34}$$

where g_0 is the magnitude of gravitational acceleration, equal to 981 m/s^2 (approximately 100 times Earth gravity), t_{rev} is a reversal time dynamically chosen for each simulation based on the mixing layer width, and Δ_{rev} is the timescale over which the reversal occurs. In each case, t_{rev} is determined when the mixing layer width h_{99}, defined as the distance between the 99% average mass fraction contours of material 1 and material 3, exceeds a predefined threshold h_{thresh}. At the time t_{thresh} at which h_{99} first exceeds h_{thresh}, the reversal time t_{rev} is defined as $t_{\text{thresh}} + 3\Delta_{\text{rev}}$, and Δ_{rev} is defined as 1600 times the computational time step. Figure 2 illustrates this process in the context of case 1, and Table III summarizes the relevant reversal parameters for each case. For cases 1 and 2, the simulation is run out to 100 ms, and in case 3, the simulation is allowed to run until h_{99} exceeds 2π.

TABLE III. Summary of parameters governing gravity reversal for each case.

Case	h_{thresh} (cm)	t_{thresh} (ms)	t_{rev} (ms)	Δ_{rev} (ms)
1	$\frac{4\pi}{3}$	32.378	35.737	1.112
2	$\frac{4\pi}{3}$	34.357	37.810	1.151
3	$\frac{11\pi}{12}$	26.078	26.935	0.286

E. RANS problem setup and initial conditions

RANS simulations are conducted utilizing several different RANS models in *Ares*. Simulations are performed on a 1D mesh with 576 uniformly spaced computational zones extending from $z = -2\pi$ to $z = 2\pi$ with nonpenetrating walls at the boundaries. Problems are set to match the LES as closely as possible with the same material densities and compositions as described in the previous section. As in the LES problem, an initial gravitational acceleration in the negative z dimension is balanced by a hydrostatic pressure gradient such that the mixing layer remains nominally centered about $z = 0$. An initial linear mass fraction profile is specified to approximately match the initial average LES mass fraction profile at each interface with an initial half-width of $h_0 = 4\Delta$. Then, at each interface at location $z = z_{\text{int}}$, we define a similarity coordinate $\chi \equiv (z - z_{\text{int}})/h_0$, which is used to specify functional distributions for the initial turbulence length scale $L_{t=0}$, the initial TKE $k_{t=0}$, the initial mass flux velocity $a_{z,t=0}$, and the initial turbulence velocity $\phi_{t=0}$:

$$L_{t=0} = \begin{cases} L_0\sqrt{1-\chi^2}, & -1 \leqslant \chi \leqslant 1 \\ 0, & \text{otherwise} \end{cases}, \tag{35a}$$

$$k_{t=0} = \begin{cases} k_0(1-\chi^2), & -1 \leqslant \chi \leqslant 1 \\ 0, & \text{otherwise} \end{cases}, \tag{35b}$$

$$a_{z,t=0} = \begin{cases} -A_{31}\sqrt{2C_{B1}k_0}(1-\chi^2), & -1 \leqslant \chi \leqslant 1 \\ 0, & \text{otherwise} \end{cases}, \tag{35c}$$

$$\phi_{t=0} = \frac{1}{2}\sqrt{k_{t=0}}. \tag{35d}$$

In Eqs. (35a) and (35b), $L_0 = 0.004$ cm, and $k_0 = 1.0 \times 10^{-10}\text{cm}^2/\mu\text{s}^2$. The initial turbulence velocity is only initialized using Eq. (35d) in the present work when utilizing the k-ϕ-L-a-$\mathcal{C}$ model. This choice for $L_0 \approx h_0/5$ is informed by prior observations by Morgan *et al.* [56] which found the integral length scale of turbulence to be approximately 20% of the mixing layer width for self-similar RT mixing. The choice for k_0 is roughly consistent with peak TKE in the comparison LES at early time (0.2 ms), and the expressions for $a_{z,t=0}$ and $\phi_{t=0}$ come from self-similarity analysis [19,23]. Note that initialization of a_z with Eq. (35c) is necessary for an accurate match to early time mixing layer growth and reduces sensitivity to the choice of k_0. Appendix B explores some initialization sensitivities using Eq. (26) for $a_{z,t=0} = 0$.

Gravity reversal in the RANS calculations follows a similar procedure as used for the LES calculations, as outlined in the previous section. That is, once the mixing layer width h_{99} exceeds the threshold given in Table III, gravitational acceleration is reversed as described by Eq. (34). For each RANS simulation t_{rev} is determined dynamically, but Δ_{rev} is

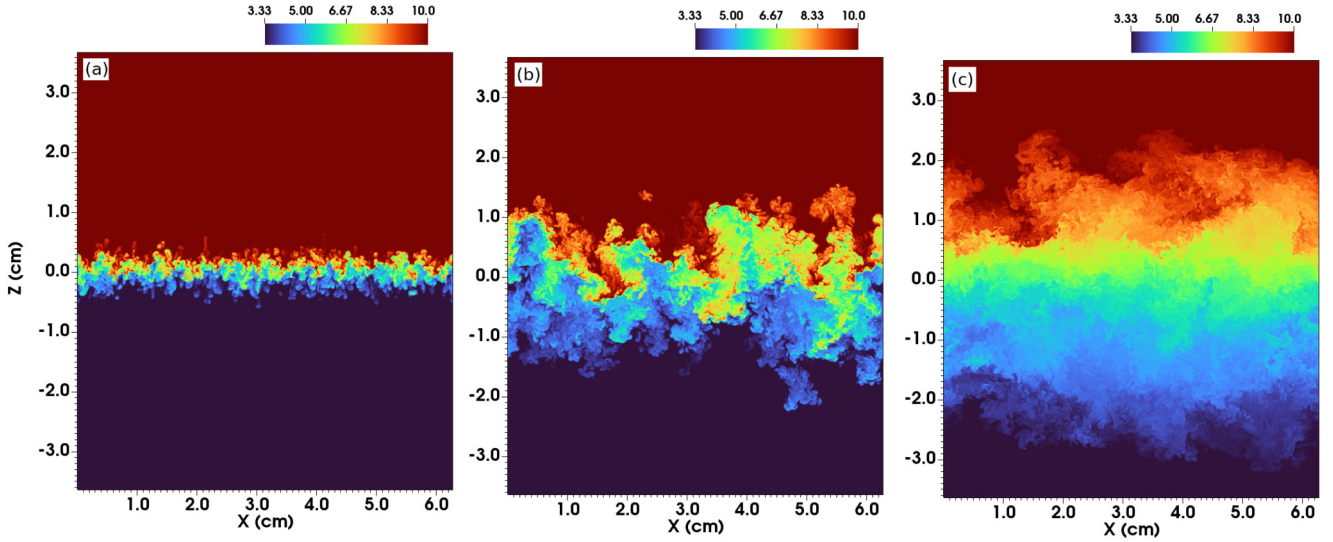

FIG. 3. Contours of density (mg/cm^3) in the $y = \pi$ plane for LES of configuration 1 at three different time instants: (a) $t = 10$ ms, (b) $t = 30$ ms, and (c) $t = 70$ ms.

set to match the value used in the comparison LES as specified in Table III. As with the LES calculations, for cases 1 and 2, RANS simulations are run out to 100 ms, and for case 3, simulations are allowed to run until h_{99} exceeds 2π.

III. RESULTS AND DISCUSSION

A. Configuration 1

Figure 3 provides a qualitative overview of the mixing layer evolution in configuration 1 by plotting contours of density from LES at several time instants. Referring back to Fig. 2, we see that Figs. 3(a) and 3(b) illustrating contours at times $t = 10$ ms and $t = 30$ ms, respectively, are from times prior to gravity reversal, while Fig. 3(c) at $t = 70$ms is taken after reversal. Together, these images illustrate how the mixing layer grows and develops into turbulence before growth is stabilized and mixing becomes more diffusive following gravity reversal. In particular, comparing Figs. 3(b) and 3(c), it is clear that following gravity reversal large turbulent structures begin to dissipate rapidly, resulting in a stable stratification and a mixing layer that is decaying towards laminarization.

Mixing layer width as a function of time is plotted for LES as well as for several RANS models in Fig. 4. Similar to observations in prior works [8,10,12], the LES mixing layer width appears to decrease by approximately 15% following gravity reversal. While this effect is sometimes referred to as "demixing," the decrease in observed mixing layer width is actually the result of the breakup and dissipation of entrained regions of nondiffusively mixed fluid [13]. By comparing LES mixing layer width against RANS, however, it is clear that the *k-L-a* [19] results using Eq. (25) as well as the BHR-3.1 [16] results both fail to capture the stabilizing effect of gravity reversal. By contrast, the BHR-4 [13] results do a better job than BHR-3.1 at capturing stabilization after gravity reversal. However, the much simpler *k-L* model [17] does as well, albeit without capturing any of the postreversal reduction in h_{99}. Results with the *k-L-a* and *k-ϕ-L-a-C* [24] models are observed to behave similar to *k-L* when the alternative buoyancy production closure given by Eq. (26) is used.

Plots in Fig. 5 provide additional insight into the dissipation of TKE and mechanisms of failure of Eq. (25) by plotting time histories of the peak TKE, k, and mass-flux velocity, a_z, across the mixing layer. First in Fig. 5(a), time evolution of k is compared between LES and RANS. It is observed in the LES that k rapidly decreases by about 80% following acceleration reversal. While all of the RANS models predict a rapid decrease in k, when Eq. (25) is utilized with the *k-L-a* model, TKE rapidly increases in a nonphysical manner shortly thereafter. When Eq. (26) is used, however, the TKE drops to zero following gravity reversal and does not grow again. The BHR models both follow a similar trajectory in their prediction of TKE which qualitatively agrees more closely with LES by remaining nonzero and decaying slowly

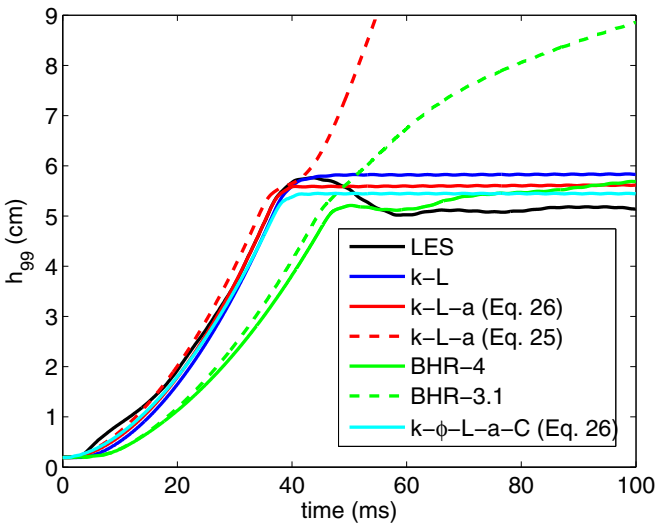

FIG. 4. Comparison between LES and RANS of mixing layer width h_{99} vs time for configuration 1.

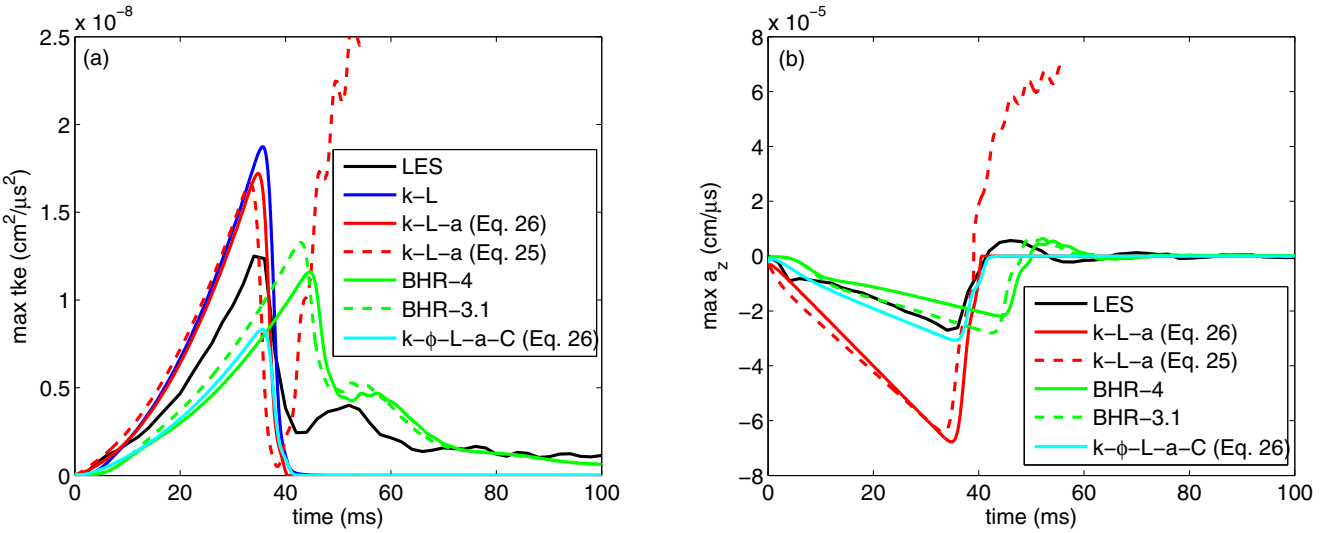

FIG. 5. Comparison between LES and RANS of time history of two turbulence variables for configuration 1: (a) maximum TKE, k, and (b) maximum mass-flux velocity, a_z.

after the initial drop following gravity reversal. Similarly, in Fig. 5(b), the time evolution of a_z is compared between LES and RANS. In the LES, a_z is observed to briefly change sign from negative to positive following gravity reversal before decaying approximately to zero. This behavior seems to be the cause of failure in the k-L-a model with Eq. (25); with Eq. (25) when a_z changes sign, buoyancy production in the k equation ($a_i \cdot \nabla \bar{p}$) becomes positive again, causing both k and a_z to continue growing. When Eq. (26) is used, however, as a_z decreases, so too does the magnitude of B_{a_j}, which causes a_z to go to zero without changing sign and thus avoids subsequent nonphysical mixing layer growth. Additionally, results utilizing the k-L-a model with Eq. (26) in Fig. 5 are exactly representative of results that would be obtained using the k-L-a-$\mathcal{C}$ model [24] since the $\mathcal{C}_{ij}$ equation becomes a passive auxiliary equation when Eq. (26) is used with the k-L-a-$\mathcal{C}$ model. It is also worth noting that the k-ϕ-L-a-$\mathcal{C}$ model more accurately predicts the peak magnitude of a_z just prior to gravity reversal than the k-L-a (or k-L-a–$\mathcal{C}$) model. Finally, it is worth commenting that while the BHR models are the only RANS results to correctly capture a brief change in sign of a_z, the BHR-3.1 model is unable to capture stabilization of the mixing layer width, and the BHR-4 model involves significantly greater increase in model complexity than what is represented by the change from Eq. (25) to Eq. (26).

The proportion of diffusively mixed fluid to entrained fluid is often represented by the so-called mixedness parameter defined as

$$\Theta_{ij} \equiv 1 - \frac{\int_{-2\pi}^{2\pi} \widetilde{Y_i'' Y_j''}\, dz}{\int_{-2\pi}^{2\pi} \widetilde{Y}_i \widetilde{Y}_j\, dz} = 1 + \frac{\int_{-2\pi}^{2\pi} \mathcal{C}_{ij}\, dz}{\int_{-2\pi}^{2\pi} \widetilde{Y}_i \widetilde{Y}_j\, dz}. \tag{36}$$

Figure 6 plots the evolution of mixedness for configuration 1 with both LES and RANS. The RANS models considered in Fig. 6 are the k-L-a-$\mathcal{C}$ and the k-ϕ-L-a-$\mathcal{C}$ models, which both solve a transport equation for the scalar mass fraction covariances $\mathcal{C}_{ij}$. When Eq. (26) is used with these models, the mixedness more or less follows the trajectory of the LES. Prior to gravity reversal, the LES and RANS results both approach the expected steady-state value of about 0.8 for RT mixing. Following gravity reversal, the RANS mixedness rapidly goes to 1, indicating near-complete dissipation of $\mathcal{C}_{13}$, while the LES results decay somewhat more slowly and oscillate around a value of about 0.98. The rapid increase in mixedness that occurs after gravity reversal, however, is consistent with previous observations in the context of Fig. 3 of the breakdown of large, entrained structures and the realization of a more diffusively mixed layer.

B. Configuration 2

Figure 7 gives a qualitative overview of the evolution of mixing in configuration 2. In this case, instabilities develop at both interfaces simultaneously, which eventually grow large enough to interact with each other and develop into a three-component mixing layer. Figures 7(a) and 7(b) illustrate density contours at two time instants prior to gravity reversal

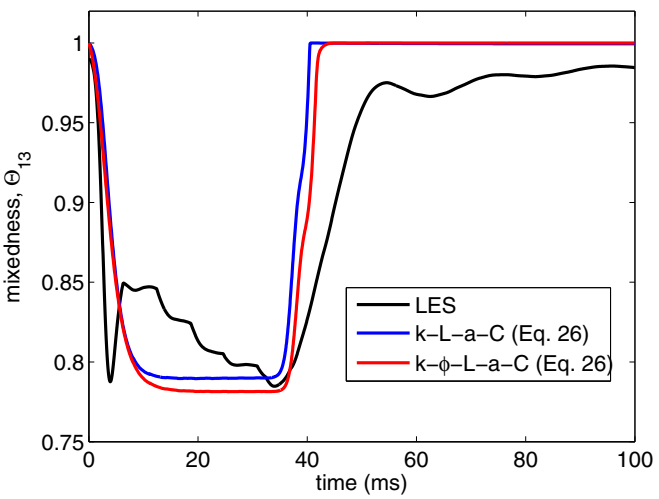

FIG. 6. Comparison between LES and RANS of mixedness Θ_{13} vs time for configuration 1.

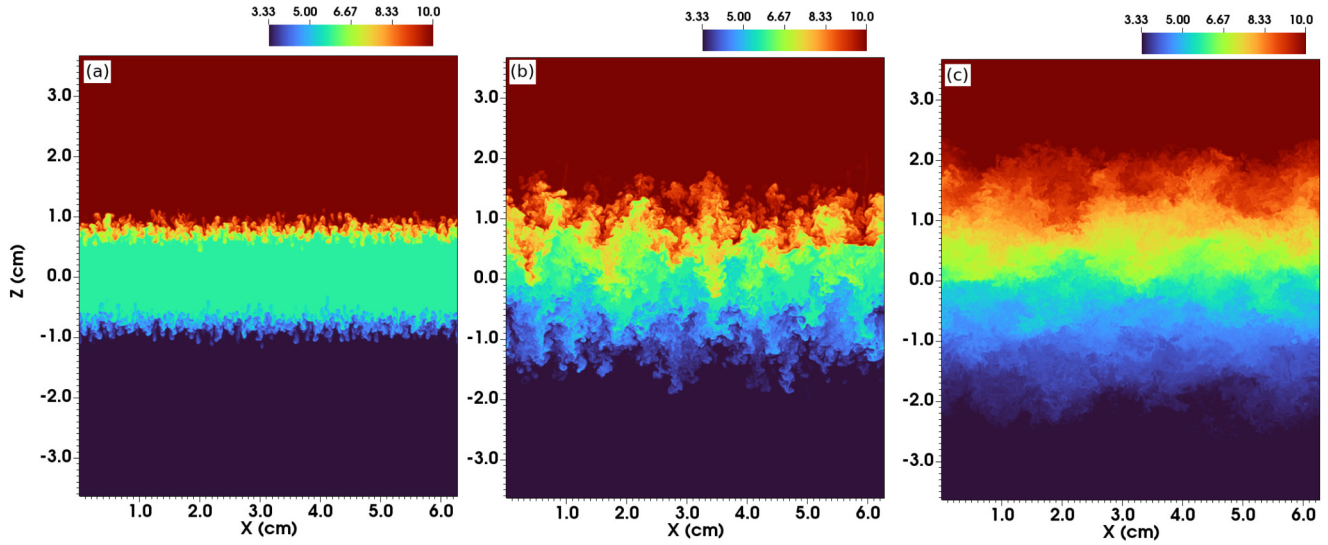

FIG. 7. Contours of density (mg/cm^3) in the $y = \pi$ plane for LES of configuration 2 at three different time instants: (a) $t = 10$ ms, (b) $t = 30$ ms, and (c) $t = 70$ ms.

(10 ms and 30 ms, respectively), while Fig. 7(c) illustrates contours after gravity reversal at 70 ms. Similar to behavior observed previously in configuration 1, large coherent structures appear to break up rapidly following gravity reversal, resulting in a mixing layer decaying towards laminarization. Additionally, comparing Fig. 3(c) with Fig. 7(c), by observing density contours alone, it is difficult to distinguish the three-component mixing layer from the two-component mixing layer after it has become well mixed.

The ability of RANS models to capture mixing layer width in configuration 2 is considered in Fig. 8. Again, compared with configuration 1, the LES result in Fig. 8 follows a similar trajectory to the LES result in Fig. 4. Specifically in LES results, the mixing layer width is observed to initially decrease following gravity reversal before stabilizing at a near-constant value. As with the two-component mixing layer, *k-L-a* results utilizing Eq. (25) and BHR-3.1 results in Fig. 8 both fail to capture mixing layer stabilization following gravity reversal. RANS results with the *k-L* model, the *k-L-a* model with Eq. (26), and the *k-ϕ-L-a-C* with Eq. (26) do all capture stabilization, although these RANS results do not capture the expected decrease in mixing layer width.

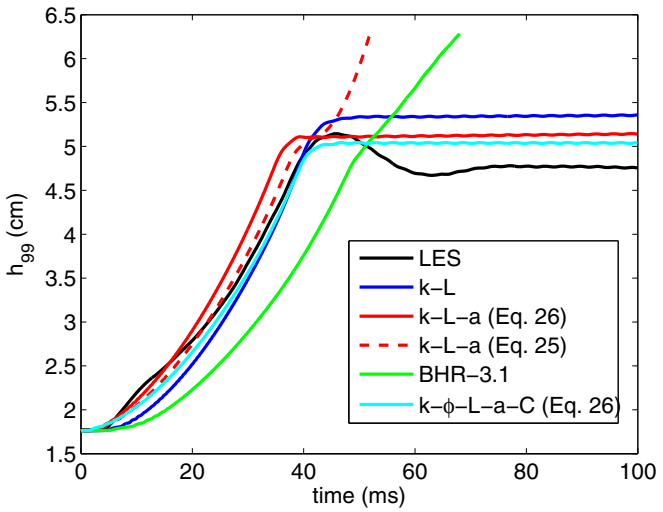

FIG. 8. Comparison between LES and RANS of mixing layer width h_{99} vs time for configuration 2.

Finally, Fig. 9 plots the evolution of mixedness quantities Θ_{12} and Θ_{13} for configuration 2 with both LES and RANS. (Due to Atwood-number symmetry of the two interfaces in configuration 2, the Θ_{23} mixedness follows a nearly identical trajectory to Θ_{12}.) Note that, due to decoupling of the b variable from the RANS model when using Eq. (26), *k-L-a-C* results in Fig. 9 follow exactly the same evolution of mixing layer width as the *k-L-a* results with Eq. (26) shown in Fig. 8. Overall, RANS results in Fig. 9 qualitatively follow a similar trend as LES. For Θ_{12}, LES mixedness initially drops to a value of about 0.8 prior to gravity reversal before rapidly increasing to reach a steady state of about 0.98. While the RANS results in Fig. 9(a) do not capture the pretransition evolution of mixedness and predict a more rapid increase in mixedness following gravity reversal, they more or less capture the qualitative behavior of the system. In Fig. 9(b), the RANS results predict a later initial drop in Θ_{13}, suggesting that spikes of material 3 are reaching into material 1 earlier in the LES than predicted by RANS. However, the magnitude of the initial drop and the subsequent rise in mixedness following gravity reversal both qualitatively agree with behavior observed in the LES.

C. Configuration 3

A qualitative overview of configuration 3 is given in Fig. 10, which again plots density contours from LES at three time instants. In this configuration, the upper interface is unstable prior to gravity reversal, while the lower interface becomes unstable following gravity reversal. This leads to a situation in which one interface is growing and the other is stabilizing at all times. Figure 10(a) illustrates the state of

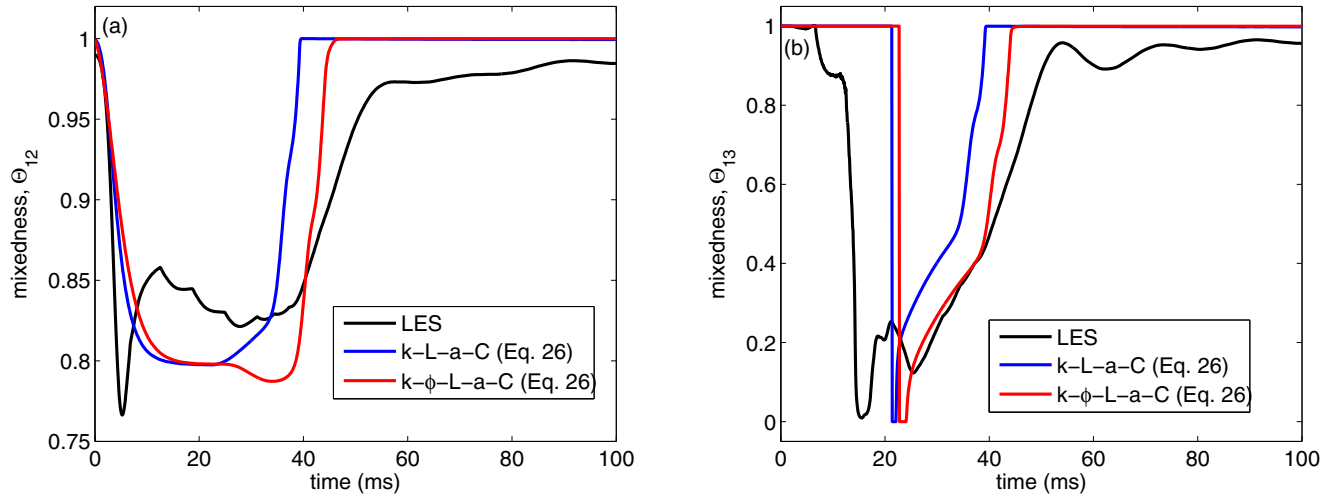

FIG. 9. Comparison between LES and RANS of mixedness vs time for configuration 2: (a) Θ_{12} and (b) Θ_{13}.

the layer prior to gravity reversal at 20 ms, while Figs. 10(b) and 10(c) both illustrate the layer at times following gravity reversal, at 40 ms and at 60 ms, respectively. As expected, Fig. 10(a) illustrates the mixing layer developing at the upper interface only, while the lower interface remains stable. In Fig. 10(b), growth at the upper interface appears to be stabilizing, with larger coherent structures breaking down into more diffusive mixing, and mixing at the lower interface appears to be accelerating. As illustrated in Fig. 10(c), the mixing layer continues to grow at the lower interface until the simulation is ended, unlike in previous simulations which stabilized following gravity reversal.

Figure 11 plots the time evolution of mixing layer width for configuration 3 with both LES and several RANS models. Using LES, the mixing layer appears to grow at a nearly constant rate, with only minor inflection indicating the time of gravity reversal. For RANS results using Eq. (25), growth generally matches LES until gravity reversal, but growth is overpredicted following gravity reversal because use of Eq. (25) fails to capture stabilization at the upper interface. Interestingly, use of Eq. (26) results in different behavior between the *k-L-a-C* and the *k-ϕ-L-a-C* models. Specifically, *k-L-a-C* results with Eq. (26) predict a nonphysically long recovery time following gravity reversal during which the upper interface rapidly stabilizes and the lower interface slowly develops. By contrast, *k-ϕ-L-a-C* results using Eq. (26) follow the LES quite closely.

The principal difference between the two RANS models considered in Fig. 11 is in the spatial profiles of turbulence quantities that are realized by the two models. Similarity analysis [19,21,23,24] predicts that the *k-L-a-C* model should give a nearly linear mass fraction profile and quadratic profiles for turbulence quantities such as k, $\mathcal{C}_{ij}$, and b. The *k-ϕ-L-a-C* model, on the other hand, is expected to give higher-order

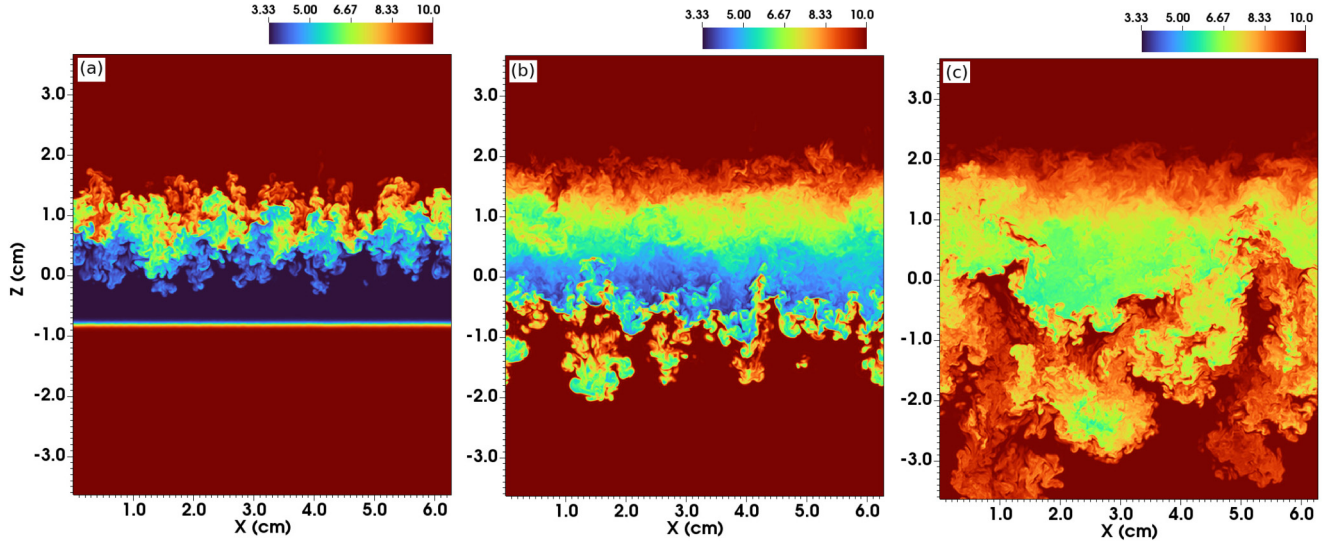

FIG. 10. Contours of density (mg/cm^3) in the $y = \pi$ plane for LES of configuration 3 at three different time instants: (a) $t = 20$ ms, (b) $t = 40$ ms, and (c) $t = 60$ ms.

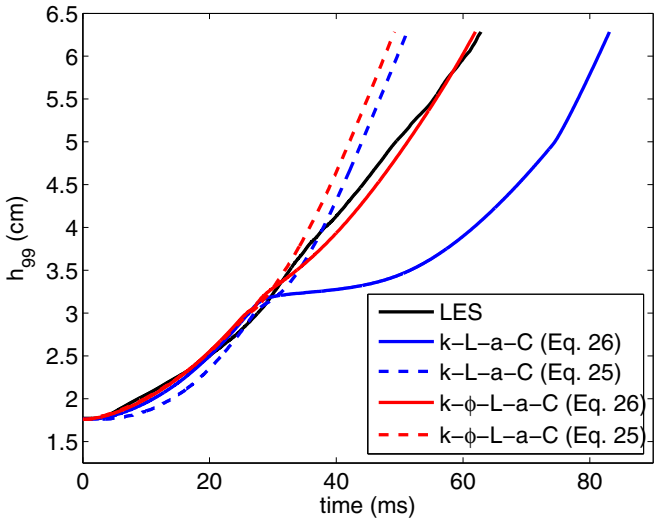

FIG. 11. Comparison between LES and RANS of mixing layer width h_{99} vs time for configuration 3.

profiles which agree better with LES, as illustrated in Fig. 12. Figure 12 plots spatial profiles of the average mass fraction of light material, $\widetilde{Y}_L$, and the density-specific-volume covariance b at $t = t_{\text{thresh}}$ just before gravity reversal. From this comparison, it is clear that the higher-order spatial profiles of the k-ϕ-L-a-$\mathcal{C}$ model agree better with LES, although the peak magnitude of b is somewhat overestimated. It is expected that accurate treatment of turbulence quantities in profile tails should be necessary for accurately matching the state of turbulence at the lower interface at the time of gravity reversal. That is, since gravity reversal occurs just after the mixing layer mixes all the way through [recall Fig. 12(a)], the state of turbulence at the lower interface at $t = t_{\text{rev}}$ is being determined by behavior in the profiles tails. Since the k-ϕ-L-a-$\mathcal{C}$ model agrees better with LES in these tails, the effective initial conditions for growth upon gravity reversal matches better as well, leading to an overall improved agreement in behavior postreversal.

The difference in behavior between the k-L-a-$\mathcal{C}$ and k-ϕ-L-a-$\mathcal{C}$ models is further clarified by Fig. 13. Figure 13 plots time histories of k and a_z at the lower interface ($z = -\pi/4$) for LES and the two RANS models. With the k-L-a-$\mathcal{C}$ model, k and a_z are observed to grow slightly at the lower interface just prior to $t = t_{\text{rev}}$. Since this growth occurs prior to gravity reversal, it is not due to buoyancy production at the interface; it is actually due to turbulent diffusion of k and a_z away from the upper interface. As observed previously in Fig. 12, the profile tails are wider with the k-L-a-$\mathcal{C}$ model, and as a result turbulence quantities transported through diffusion from the upper interface are observed to arrive at the lower interface earlier than with the k-ϕ-L-a-$\mathcal{C}$ model. A consequence of this behavior is that the magnitude of B_{a_j} at the time of gravity reversal is greater with the k-L-a-$\mathcal{C}$ model than with the k-ϕ-L-a-$\mathcal{C}$ model, and it acts as a sink term immediately following gravity reversal. As a result, the k-L-a-$\mathcal{C}$ is observed to take a longer period of time to redevelop turbulence at the lower interface and resume growing the mixing layer.

IV. SUMMARY AND CONCLUSIONS

The present work has examined the behavior of Rayleigh-Taylor mixing following sudden acceleration reversal in three geometrical configurations. In each configuration, high-fidelity LES results have been compared against 1D RANS simulations as a means to evaluate the capacity of particular RANS formulations to capture the dynamics of mixing under complex acceleration history. In the first configuration, a canonical, two-component RT mixing layer is subjected to a sudden reversal of gravity, which results in a stabilization of the mixing layer and a decay of entrained turbulent structures to more diffusive mixing. In the second configuration, a three-component RT mixing layer with two unstable interfaces develops until there is significant three-component mixing before it is subjected to a reversal of gravity, resulting in a similar stabilization and decay towards diffusive mixing. Finally in the third configuration, a light layer is interposed between two heavy layers, resulting in a situation in which only the top

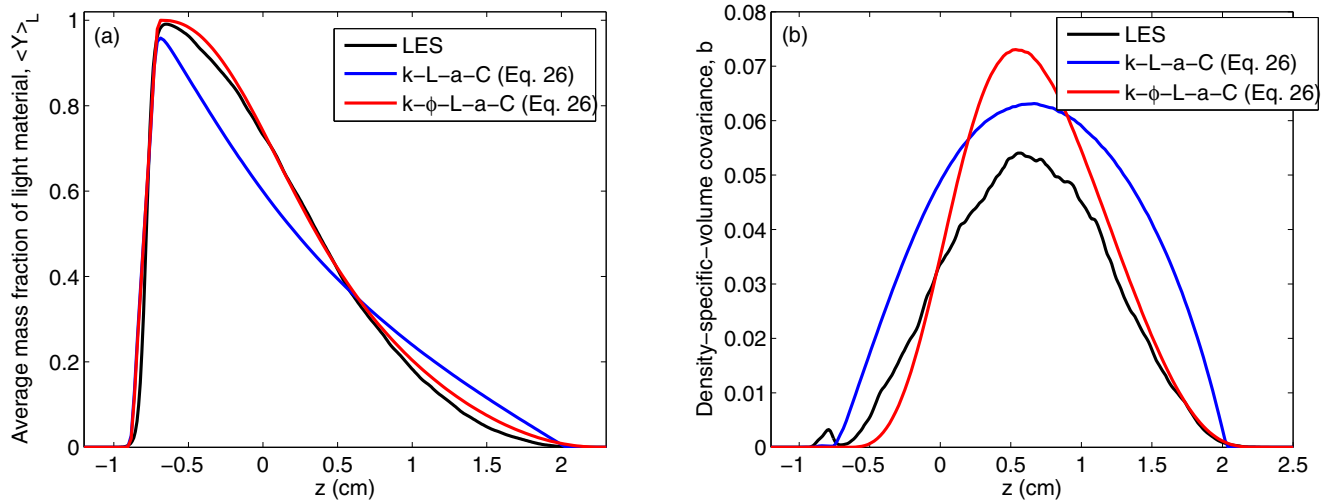

FIG. 12. Comparison between LES and RANS of spatial profiles at $t = t_{\text{thresh}}$ in configuration 3: (a) average mass fraction of light material, $\widetilde{Y}_L$, and (b) the density-specific-volume covariance b.

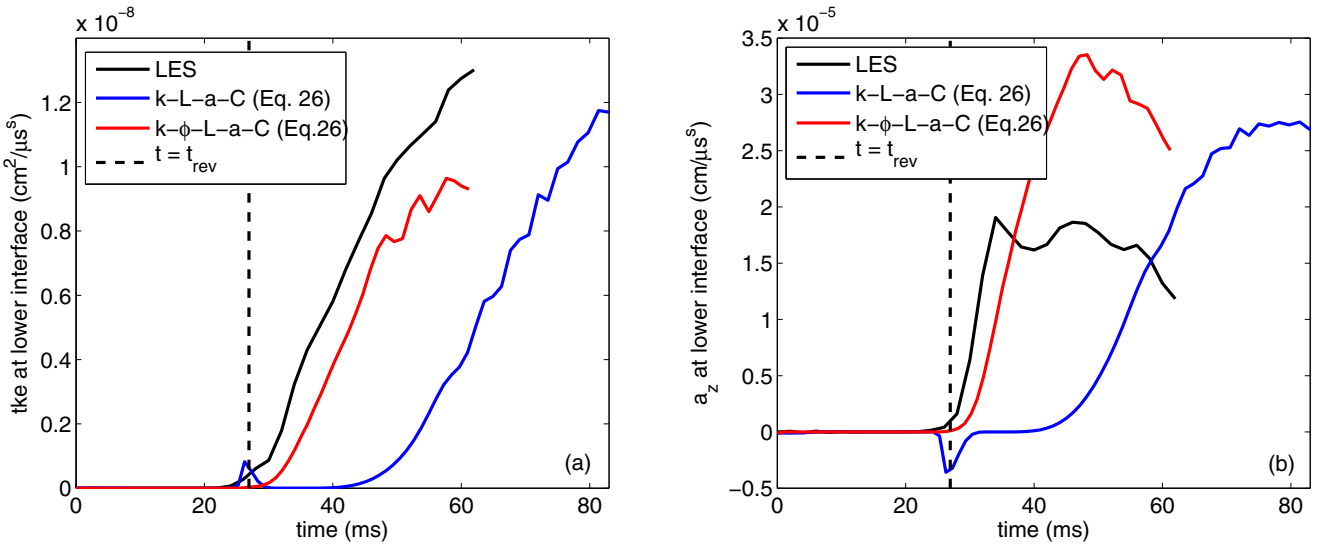

FIG. 13. Comparison between LES and RANS of time history of two turbulence variables in configuration 3 at the lower interface ($z = -\pi/4$): (a) TKE, k, and (b) mass-flux velocity, a_z. Reversal time t_{rev} is indicated for reference with a dashed black line.

interface is initially unstable, but following gravity reversal the top interface stabilizes while the bottom interface grows unstably.

In studying the first configuration, it was found that while the older k-L model was capable of capturing the mixing layer stabilization effect of gravity reversal, the newer k-L-a model continued to grow the mixing layer in a nonphysical way. The cause of this nonphysical behavior with the k-L-a model was determined to have been the buoyancy production term in the a_j equation [Eq. (25)], which can lead to a change in the sign of a_z and a nonphysical continuation of mixing layer growth postreversal. An alternative closure for buoyancy production was suggested [Eq. (26)] which was shown to recover the expected stabilization when used with the k-L-a model. When used with the k-L-a-$\mathcal{C}$ and k-ϕ-L-a-$\mathcal{C}$ models, the alternative closure allowed the models to approximately capture time history of the mixedness as well.

Consideration of the second configuration enabled assessment of RANS model behavior under the conditions of three-component mixing. Generally speaking, the three-component mixing layer was observed to evolve in a manner similar to the two-component mixing layer. As before, the k-L-a model with Eq. (25) was found to predict significant nonphysical growth following gravity reversal, while the k-L model and models utilizing Eq. (26) were found to stabilize mixing layer growth. Despite a later initial drop in Θ_{13} observed by RANS models, suggesting a discrepancy in the onset of three-component mixing, reasonable qualitative agreement with LES was observed in Θ_{12} and Θ_{13} mixedness histories for the k-L-a-$\mathcal{C}$ and k-ϕ-L-a-$\mathcal{C}$ models when used with Eq. (26).

The third configuration proved to be most challenging and perhaps the best discriminator amongst RANS models. In this case, RANS simulation with Eq. (25) resulted in a similar overprediction of growth following gravity reversal with both the k-L-a-$\mathcal{C}$ and k-ϕ-L-a-$\mathcal{C}$ models. However, when Eq. (26) was used with these models, only the k-ϕ-L-a-$\mathcal{C}$ model agreed well with LES. When Eq. (26) was used with the k-L-a-$\mathcal{C}$ model in configuration 3, a nonphysically long recovery period was required before the RANS result recovered the expected growth rate. The ability of the RANS model to match profiles of turbulence quantities in the tails is believed to be important to matching conditions at the lower interface at the time of gravity reversal. The high-order spatial profiles of the k-ϕ-L-a-$\mathcal{C}$ model, which were shown to agree more closely with LES than the k-L-a-$\mathcal{C}$ model, are therefore believed to have contributed to a more-accurate prediction in mixing layer width versus time.

The present work has not spent too much time discussing the BHR-4 model [13], other than to show that it more or less behaves as expected for configuration 1 and represents an alternative approach to capturing mixing layer stabilization following gravity reversal. Indeed, the BHR models gave the best prediction of any considered in terms of the ability of these models to capture physical sign change of a_z and a more realistic decay of TKE following gravity reversal. These qualities must be attributed at least partially to dissipation of b in the BHR models preventing Eq. (25) from growing unbounded. While the BHR-4 model is able to capture mixing layer stabilization following gravity reversal more successfully than the BHR-3.1 model, it does so with significant increase in model complexity. Changing buoyancy production in the a equation from Eq. (25) to Eq. (26) is a much more modest change that can be done to capture the most significant impact of gravity reversal, which is the stabilization of mixing layer width.

Overall, this work has shown that RANS models relying on a commonly used transport equation for mass-flux velocity may behave nonphysically for turbulent mixing involving rapid acceleration reversals. Since ICF applications frequently involve complex acceleration histories, the present results suggest close scrutiny is warranted, as some commonly used RANS models may be prone to over-predicting the impact of turbulent mixing. An alternative formulation for buoyancy production in the mass-flux velocity equation was proposed, and models using this formulation were demonstrated to more

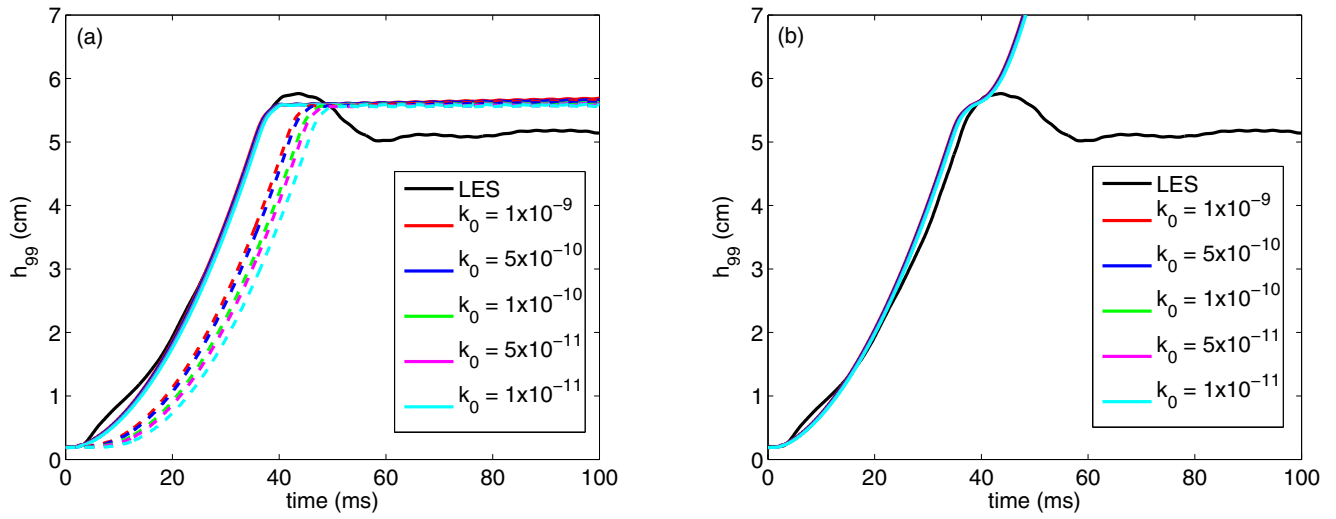

FIG. 14. Exploration of RANS solution sensitivity to initialization of k and a_z in configuration 1: (a) Mixing layer width h_{99} vs time for k-L-a model using Eq. (26) with several choices for k_0 when $a_{z,t=0}$ is given by Eq. (35c) (solid lines) and when $a_{z,t=0} = 0$ (dashed lines). (b) Mixing layer width h_{99} vs time for k-L-a model using Eq. (25) with several choices for k_0 when $a_{z,t=0} = 0$.

accurately capture mixing layer stabilization following gravity reversal. When used with the k-ϕ-L-a-$\mathcal{C}$ model, this new formulation best matched LES for all three configurations considered. Of course, more work remains to be done. The behavior of Eq. (26) should be evaluated in simulations of actual experiments such as those by Dimonte, Ramaphrabhu, and Andrews [7], and it should be evaluated in mixing applications driven primarily by Richtmyer-Meshkov instability. In RT-stable configurations such as a shock passing from a heavy fluid into light fluid, use of Eq. (26) should lead to a dissipation of k and a_j where use of Eq. (25) will not. Therefore, some measure of shock detection is likely required to keep buoyancy production of k positive within shocks when using Eq. (26), as is often done with other models such as the k-L model [17]. Similarly, the alternative formulation given by Eq. (26) should be evaluated in more realistic ICF simulations and in configurations involving more complex acceleration histories such as "accel-decel-accel." Improvements to better capture the reduction in mixing layer width (i.e., "demixing") and the physical change in sign of a_z following gravity reversal should be pursued as well.

ACKNOWLEDGMENTS

The author would like to thank Mark Ulitsky, Peter Rambo, Britton Olson, Oleg Schilling, Brian Pudliner, and other colleagues at LLNL for their helpful input and discussions in preparation of this work. This work was performed under the auspices of the U.S. Department of Energy by Lawrence Livermore National Laboratory under Contract No. DE-AC52-07NA27344.

APPENDIX A: ADDITIONAL SELF-SIMILARITY ANALYSIS FOR THE k-ϕ-L-a-$\mathcal{C}$ MODEL

When Eq. (26) is utilized to close buoyancy production in k-L-a-based models (such as k-L-a, k-$2L$-a, k-L-a-V, etc.), no additional impact is realized to previously derived self-similarity constraints for model coefficients as long as $C_{B2} = 1$. In newer models such as the k-ϕ-L-a-V [23] and k-ϕ-L-a-$\mathcal{C}$ [24] models, in which an additional transport equation for the turbulence velocity ϕ is utilized, a more complicated constraint on C_{B2} is derived.

Following the same approach to self-similarity analysis described in detail in previous work [23], the reduced a equation when utilizing Eq. (26) becomes

$$\dot{A}_0 = -\left(C_A + \frac{4A\beta}{3\gamma V_0^{3/8}}\frac{K_0}{A_0P_0} + \frac{C_{L1}}{2}\right)\frac{A_0P_0}{L_0} - C_{B2}\frac{A_0^2}{K_0}g. \tag{A1}$$

In Eq. (A1) the dot notation has been used to indicate differentiation with respect to time, and γ is a normalization constant given by

$$\gamma = \sqrt{\pi}\frac{\Gamma\left(\frac{5}{2}\right)}{\Gamma(3)} \approx 1.178. \tag{A2}$$

A_0, V_0, P_0, L_0, and K_0 are the time-dependent self-similar functions defined by the separability ansatz

$$k(\chi,t) = K_0(t)f^{5/2}(\chi), \tag{A3a}$$
$$\phi(\chi,t) = P_0(t)f^{1/2}(\chi), \tag{A3b}$$
$$L(\chi,t) = L_0(t)f^{1/2}(\chi), \tag{A3c}$$
$$a(\chi,t) = A_0(t)f^{5/2}(\chi), \tag{A3d}$$
$$\mathcal{C}_{12}(\chi,t) = -V_0(t)f^{4}(\chi). \tag{A3e}$$

Finally, β in Eq. (A1) is the proportionality constant relating the turbulence length scale to the mixing layer width h such that $L_0 = \beta h$. To derive a constraint on the coefficient C_{B2}, it is assumed that A_0 and P_0 should be related through an additional proportionality constant such that $A_0 = C_aP_0$. From prior work [23], the reduced ϕ equation is then derived as

$$\dot{P}_0 = \left(C_{p1} - \frac{C_{L1}}{2}\right)\frac{P_0^2}{L_0} - C_{p3}\frac{A_0}{P_0V_0^{3/8}}g, \tag{A4}$$

where C_{p1} and C_{p3} are additional model coefficients appearing in the ϕ equation. In order to satisfy the assumed proportionality between A_0 and P_0, Eqs. (A1) and (A4) must reduce to the same form. Thus, the following constraint can be derived:

$$C_{B2} = \frac{C_{p3}}{V_0^{3/8}} \frac{K_0}{P_0^2}. \tag{A5}$$

Following the same approach as in previous work [23], an ansatz of self-similar RT growth can be invoked such that $h = \alpha A g t^2$ for the RT growth parameter α. Then for $C_a = -2A\sqrt{C_{B1}}$, the following expression is obtained for α:

$$\alpha = \frac{C_{p3} C_{L1}}{10 V_0^{3/8} \gamma N_L \left(3 - 4\frac{C_{p1}}{C_{L1}}\right)}. \tag{A6}$$

Utilizing Eq. (A6) and following the same procedure laid out in Sec. III A 5 of the previous work [23], it is possible to derive

$$\frac{K_0}{P_0^2} = \frac{V_0^{3/8}\left(3 - 4\frac{C_{p1}}{C_{L1}}\right)}{4C_{p3}\left(\frac{C_D}{C_{L1}} + 1\right)}. \tag{A7}$$

Finally, by substituting Eq. (A7) back into Eq. (A5), a complete constraint is derived for C_{B2}:

$$C_{B2} = \frac{\left(3 - 4\frac{C_{p1}}{C_{L1}}\right)}{4\left(\frac{C_D}{C_{L1}} + 1\right)}. \tag{A8}$$

Note that in this case in which Eq. (26) is used with the k-ϕ-L-a-$\mathcal{C}$ model, C_{B2} will not necessarily equal unity, but C_{p3} becomes a free parameter controlling the ratio between $\sqrt{K_0}$ and P_0 for buoyancy-driven flow.

APPENDIX B: INITIALIZATION SENSITIVITY

Figure 14 explores RANS sensitivity to choice of initial k and a_z in configuration 1. In Fig. 14(a), k_0 is varied by two orders of magnitude under two different initialization approaches for a_z when using the k-L-a model with Eq. (26.) When a_z is initialized according to Eq. (35c) [solid lines in Fig. 14(a)], the predicted mixing layer width shows little sensitivity to k_0 and agrees well with LES. On the other hand, when $a_{z,t=0} = 0$ [dashed lines in Fig. 14(a)], the result shows increased sensitivity to the choice of k_0, and early-time agreement with LES is poor; although, the rate of growth appears to be recovered at later time. In contrast, Fig. 14(b) illustrates mixing layer width predicted using Eq. (25) for several choices of k_0 when $a_{z,t=0} = 0$. With Eq. (25), the solution is less sensitive to choice of k_0 for $a_{z,t=0} = 0$.

In the case of Eq. (26) when $a_{z,t=0} = 0$, early-time growth of a_j is driven by the shear production term in Eq. (24) rather than the buoyancy production term. When a_z is initialized with Eq. (35c), however, the buoyancy production term drives growth at early time, and sensitivity to k_0 is reduced. When Eq. (25) is used, early-time growth of a_j is always driven by the buoyancy production term even when $a_{z,t=0} = 0$. Therefore one must be careful to consider initial conditions for a_z when using Eq. (26), as use of this form may lead to increased solution sensitivity compared with Eq. (25), particularly when $a_j = 0$.

[1] Y. Zhou, Rayleigh-Taylor and Richtmyer-Meshkov instability induced flow, turbulence, and mixing. I, Phys. Rep. **720–722**, 1 (2017).

[2] Y. Zhou, Rayleigh–Taylor and Richtmyer–Meshkov instability induced flow, turbulence, and mixing. II, Phys. Rep. **723–725**, 1 (2017).

[3] V. A. Smalyuk, M. Barrios, J. A. Caggiano, D. T. Casey, C. J. Cerjan, D. S. Clark, M. J. Edwards, J. A. Frenje, M. Gatu-Johnson, V. Y. Glebov *et al.*, Hydrodynamic instability growth and mix experiments at the National Ignition Facility, Phys. Plasmas **21**, 056301 (2014).

[4] V. A. Smalyuk, R. E. Tipton, J. E. Pino, D. T. Casey, G. P. Grim, B. A. Remington, D. P. Rowley, S. V. Weber, M. Barrios, L. R. Benedetti *et al.*, Measurements of an Ablator-Gas Atomic Mix in Indirectly Driven Implosions at the National Ignition Facility, Phys. Rev. Lett. **112**, 025002 (2014).

[5] R. S. Craxton, K. S. Anderson, T. R. Boehly, V. N. Goncharov, D. R. Harding, J. P. Knauer, R. L. McCrory, P. W. McKenty, D. D. Meyerhofer, J. F. Myatt *et al.*, Direct-drive inertial confinement fusion: A review, Phys. Plasmas **22**, 110501 (2015).

[6] D. Winske, The magnitized Rayleigh-Taylor instability with a temporally variable gravity, Phys. Plasmas **4**, 2454 (1997).

[7] G. Dimonte, P. Ramaprabhu, and M. Andrews, Rayleigh-Taylor instability with complex acceleration history, Phys. Rev. E **76**, 046313 (2007).

[8] P. Ramaprabhu, V. Karkhanis, and A. G. W. Lawrie, The Rayleigh-Talor instability driven by an accel-decel-accel profile, Phys. Fluids **25**, 115104 (2013).

[9] P. Ramaprabhu, V. Karkhanis, R. Banerjee, H. Varshochi, M. Khan, and A. G. W. Lawrie, Evolution of the single-mode Rayleigh-Taylor instability under the influence of time-dependent accelerations, Phys. Rev. E **93**, 013118 (2016).

[10] D. Aslangil, A. Banerjee, and A. G. W. Lawrie, Numerical investigation of initial condition effects on Rayleigh-Taylor instability with acceleration reversals, Phys. Rev. E **94**, 053114 (2016).

[11] D. Aslangil, Z. Farley, A. G. W. Lawrie, and A. Banerjee, Rayleigh-Taylor instability with varying periods of zero acceleration, ASME J. Fluids Eng. **142**, 121103 (2020).

[12] D. Livescu, T. Wei, and P. T. Brady, Rayleigh-Taylor instability with gravity reversal, Physica D **417**, 132832 (2021).

[13] N. O. Braun and R. A. Gore, A multispecies turbulence model for the mixing and de-mixing of miscible fluids, J. Turbul. **22**, 784 (2021).

[14] D. C. Besnard, F. H. Harlow, R. M. Rauenzahn, and C. Zemach, Turbulence transport equations for variable-density turbulence and their relationship to two-field models, Tech. Rep. LAUR-12303 (Los Alamos National Laboratory, 1992).

[15] J. D. Schwarzkopf, D. Livescu, R. A. Gore, R. M. Rauenzahn, and J. R. Ristorcelli, Application of a second-moment closure

model to mixing processes involving multicomponent miscible fluids, J. Turbul. **12**, N49 (2011).

[16] J. D. Schwarzkopf, D. Livescu, J. R. Baltzer, R. A. Gore, and J. R. Ristorcelli, A two-length scale turbulence model for single-phase multi-fluid mixing, Flow, Turbul. Combust. **96**, 1 (2016).

[17] G. Dimonte and R. Tipton, K-L turublence model for the self-similar growth of the Rayleigh-Taylor and Richtmyer-Meshkov instabilities, Phys. Fluids **18**, 085101 (2006).

[18] B. E. Morgan and J. A. Geenough, Large-eddy and unsteady RANS simulations of a shock-accelerated heavy gas cylinder, Shock Waves **26**, 355 (2016).

[19] B. E. Morgan and M. E. Wickett, Three-equation model for the self-similar growth of Rayleigh-Taylor and Richtmyer-Meshkov instabilities, Phys. Rev. E **91**, 043002 (2015).

[20] B. E. Morgan, O. Schilling, and T. A. Hartland, Two-length-scale turbulence model for self-similar buoyancy-, shock-, and shear-driven mixing, Phys. Rev. E **97**, 013104 (2018).

[21] B. E. Morgan, B. J. Olson, W. J. Black, and J. A. McFarland, Large-eddy simulation and Reynolds-averaged Navier-Stokes modeling of a reacting Rayleigh-Taylor mixing layer in a spherical geometry, Phys. Rev. E **98**, 033111 (2018).

[22] B. E. Morgan, Scalar mixing in a Kelvin-Helmholtz shear layer and implications for Reynolds-averaged Navier-Stokes modeling of mixing layers, Phys. Rev. E **103**, 053108 (2021).

[23] B. E. Morgan, Self-consistent, high-order spatial profiles in a model for two-fluid turbulent mixing, Phys. Rev. E **104**, 015107 (2021).

[24] B. E. Morgan, Simulation and Reynolds-averaged Navier-Stokes modeling of a three-component Rayleigh-Taylor mixing problem with thermonuclear burn, Phys. Rev. E **105**, 045104 (2022).

[25] A. W. Cook, W. Cabot, and P. L. Miller, The mixing transition in Rayleigh-Taylor instability, J. Fluid Mech. **511**, 333 (2004).

[26] W. H. Cabot and A. W. Cook, Reynolds number effects on Rayleigh-Taylor instability with possible implications for type Ia supernovae, Nat. Phys. **2**, 562 (2006).

[27] B. J. Olson and A. W. Cook, Rayleigh-Taylor shock waves, Phys. Fluids **19**, 128108 (2007).

[28] B. J. Olson, J. Larsson, S. K. Lele, and A. W. Cook, Non-linear effects of the combined Rayleigh-Taylor/Kelvin-Helmholtz instability, Phys. Fluids **23**, 114107 (2011).

[29] V. K. Tritschler, B. J. Olson, S. K. Lele, S. Hickel, X. Y. Hu, and N. A. Adams, On the Richtmyer-Meshkov instability evolving from a deterministic multimode planar interface, J. Fluid Mech. **755**, 429 (2014).

[30] B. J. Olson and J. Greenough, Large eddy simulation requirements for the Richtmyer-Meshkov instability, Phys. Fluids **26**, 044103 (2014).

[31] B. J. Olson and J. Greenough, Comparison of two- and three-dimensional simulations of miscible Richtmyer-Meshkov instability with multimode initial conditions, Phys. Fluids **26**, 101702 (2014).

[32] A. Campos and B. E. Morgan, Direct numerical simulation and Reynolds-averaged Navier-Stokes modeling of the sudden viscous dissipation for multicomponent turbulence, Phys. Rev. E **99**, 063103 (2019).

[33] A. W. Cook, Artificial fluid properties for large-eddy simulation of compressible turbulent mixing, Phys. Fluids **19**, 055103 (2007).

[34] A. W. Cook, Enthalpy diffusion in multicomponent flows, Phys. Fluids **21**, 055109 (2009).

[35] B. E. Morgan and W. J. Black, Parametric investigation of the transition to turbulence in Rayleigh-Taylor mixing, Physica D **402**, 132223 (2020).

[36] R. W. Sharp and R. T. Barton, HEMP advection model, Report UCID 17809 (Lawrence Livermore Laboratory, Livermore, CA, 1981).

[37] R. M. Darlington, T. L. McAbee, and G. Rodrigue, A study of ALE simulations of Rayleigh-Taylor instability, Comput. Phys. Commun. **135**, 58 (2001).

[38] Tz. V. Kolev and R. N. Rieben, A tensor artificial viscosity using a finite element approach, J. Comput. Phys. **228**, 8336 (2009).

[39] M. J. Berger and J. Oliger, Adaptive mesh refinement for hyperbolic partial differential equations, J. Comput. Phys. **53**, 484 (1984).

[40] M. J. Berger and P. Colella, Local adaptive mesh refinement for shock hydrodynamics, J. Comput. Phys. **82**, 64 (1989).

[41] K. S. Raman, O. A. Hurrican, H.-S. Park, B. A. Remington, H. Robey, V. A. Smalyuk, R. P. Drake, C. M. Krauland, C. C. Kuranz, J. F. Hansen, and E. C. Harding, Three-dimensional modeling and analysis of a high energy density Kelvin-Helmholtz experiment, Phys. Plasmas **19**, 092112 (2012).

[42] D. T. Casey, V. A. Smalyuk, R. E. Tipton, J. E. Pino, G. P. Grim, B. A. Remington, D. P. Rowley, S. V. Weber, M. Barrios, L. R. Benedetti *et al.*, Development of the CD Symcap platform to study gas-shell mix in implosions at the National Ignition Facility, Phys. Plasmas **21**, 092705 (2014).

[43] S. V. Weber, D. T. Casey, D. C. Eder, J. D. Kilkenny, J. E. Pino, V. A. Smalyuk, G. P. Grim, B. A. Remington, D. P. Rowley, C. B. Yeamans *et al.*, Simulations of indirectly driven gas-filled capsules at the National Ignition Facility, Phys. Plasmas **21**, 112706 (2014).

[44] S. F. Khan, S. A. MacLaren, J. D. Salmonson, T. Ma, G. A. Kyrala, J. E. Pino, J. R. Rygg, J. E. Field, R. Tommasini, J. E. Ralph *et al.*, Symmetry tuning of a near one-dimensional 2-shock platform for code validation at the National Ignition Facility, Phys. Plasmas **23**, 042708 (2016).

[45] M. Gatu Johnson, A. B. Zylstra, A. Bacher, C. R. Brune, D. T. Casey, C. Forrest, H. W. Hermann, M. Hohenberger, D. B. Sayre, R. M. Bionta *et al.*, Development of an inertial confinement fusion platform to study charged-particle-producing nuclear reactions relevant to nuclear astrophysics, Phys. Plasmas **24**, 041407 (2017).

[46] M. Gatu Johnson, D. T. Casey, M. Hohenberger, A. B. Zylstra, A. Bacher, C. R. Brune, R. M. Bionta, R. S. Craxton, C. L. Ellison, M. Farrell *et al.*, Optimization of a high-yield, low-areal-density fusion product source at the National Ignition Facility with applications in nucleosynthesis experiments, Phys. Plasmas **25**, 056303 (2018).

[47] J. D. Bender, O. Schilling, K. S. Raman, R. A. Managan, B. J. Olson, S. R. Copeland, C. L. Ellison, D. J. Erskine, C. M. Huntington, B. E. Morgan *et al.*, Simulation and flow physics of a shocked and reshocked high-energy-density mixing layer, J. Fluid Mech. **915**, A84 (2021).

[48] A. Banerjee, R. A. Gore, and M. J. Andrews, Development and validation of a turbulent-mix model for variable-density and compressible flows, Phys. Rev. E **82**, 046309 (2010).

[49] N. A. Denissen, B. Rollin, J. M. Reisner, and M. J. Andrews, The tilted rocket rig: A Rayleigh-Taylor test case for RANS models, J. Fluids Eng.–T. ASME **136**, 091301 (2014).

[50] I. W. Kokkinakis, D. Drikakis, D. L. Youngs, and R. J. R. Williams, Two-equation and multi-fluid turbulence models for Rayleigh-Taylor mixing, Int. J. Heat Fluid Flow **56**, 233 (2015).

[51] I. W. Kokkinakis, D. Drikakis, and D. L. Youngs, Modeling of Rayleigh-Taylor mixing using single-fluid models, Phys. Rev. E **99**, 013104 (2019).

[52] I. W. Kokkinakis, D. Drikakis, and D. L. Youngs, Two-equation and multi-fluid turbulence models for Richtmyer-Meshkov mixing, Phys. Fluids **32**, 074102 (2020).

[53] M. Xiao, Y. Zhang, and B. Tian, Unified prediction of reshocked Richtmyer-Meshkov mixing with K-L model, Phys. Fluids **32**, 032107 (2020).

[54] M. Xiao, Y. Zhang, and B. Tian, Modeling of turbulent mixing with an improved K-L model, Phys. Fluids **32**, 092104 (2020).

[55] S. Gauthier and M. Bonnet, A k-ε model for turbulent mixing in shock-tube flows induced by Rayleigh-Taylor instability, Phys. Fluids A: Fluid Dynam. **2**, 1685 (1990).

[56] B. E. Morgan, B. J. Olson, J. E. White, and J. A. McFarland, Self-similarity of a Rayleigh-Taylor mixing layer at low Atwood number with a multimode initial perturbation, J. Turbul. **18**, 973 (2017).